3D real-time indoor localization via broadband nonlinear backscatter in passive devices with centimeter precision

3 authors:

Yunfei Ma
Massachusetts Institute of Technology
21 PUBLICATIONS   **552** CITATIONS

SEE PROFILE

Xiaonan Hui
Cornell University
42 PUBLICATIONS   **1,396** CITATIONS

SEE PROFILE

Edwin C. Kan
Cornell University
252 PUBLICATIONS   **3,966** CITATIONS

SEE PROFILE

Some of the authors of this publication are also working on these related projects:

Project   Non-logic Devices in Logic CMOS Processes View project

Project   US Department of Energy's Advanced Research Projects Agency-Energy (ARPA-E) under award number DE-AR0000528 View project

3D Real-time Indoor Localization via Broadband Nonlinear Backscatter in Passive Devices with Centimeter Precision

Yunfei Ma
School of ECE, Cornell
University
Ithaca, New York 14853
ym274@cornell.edu

Xiaonan Hui
School of ECE, Cornell
University
Ithaca, New York 14853
xh273@cornell.edu

Edwin C. Kan
School of ECE, Cornell
University
Ithaca, New York 14853
eck5@cornell.edu

ABSTRACT

We propose and demonstrate accurate 3D real-time indoor localization via broadband nonlinear backscatter in passive devices. The proposed method does not need any relative motion between a reader and a tag or the use of reference anchor nodes. In the conventional radio frequency identification (RFID) system, a passive tag responds to a reader by switching its antenna "on"and "off". The operation of such conventional backscatter is essentially "linear", since the reader-to-tag (downlink) and tag-to-reader (uplink) signals overlap on the same carrier frequency. Although linear backscatter is straightforward, the self-jamming problem caused by strong leakage signals from the transmitter to the receiver is notorious and poses many constraints on the received signal quality, operation bandwidth, modulation flexibility and system complexity. To enable high-accuracy real-time 3D indoor localization for passive devices, we show that nonlinear backscatter is more effective than linear backscatter. Nonlinear backscatter exploits nonlinear elements in passive devices to generate second or higher-order harmonics as the uplink response. Separation of downlink and uplink on different carriers allows immediate self-jamming cancellation and direct un-modulated carrier phase decoding, hence resulting in better received signal quality and broad bandwidth of operation, both of which are critical for the localization system. The broad bandwidth allows the design of an efficient phase-based ranging algorithm - heuristic multi-frequency continuous wave (HMFCW) ranging which resolves ambiguous phase cycles with heuristically optimized sparse carrier frequencies. HMFCW ranging can correctly pin down the phase cycle integer with 100% reliability as long as the phase error falls within $\pm 90° \times$BW% (percentage bandwidth). In our present implementation, we achieved a median ranging error below 1 cm under phase error bounds of $\pm 50°$. We realized real-time 3D localization from differential ranging by nonlinear conjugate gradient (CG) search for hyperboloids intersection in a multi-static transceiving system with 1 Tx antenna and 4 Rx antennas. The measured 3D localization median er-

ror was 3.5 cm in the indoor environment. Presently, the measurement latency was less than 0.155 seconds. We will present system design, algorithms and a prototype with experimental evaluation.

Categories and Subject Descriptors

C.2 [**Computer Systems Organization**]: Computer Communications Networks

Keywords

3D localization; RFID; real-time; nonlinear backscatter; human machine interface

1. INTRODUCTION

The Internet of Things (IoT) requires proximity intelligence for many of its applications, especially for identification and localization [1, 3, 8, 9, 10]. A passive tag that can operate without a battery is free of maintenance and ideal to be attached to any articles as the last layer in IoT [2]. High-accuracy localization and tracking around centimeter accuracy level is highly desirable for these passive devices in order to enable new motion tracking systems [6, 7], accurate robotic feedback [10] for object fetching and delivery, and gesture acquisition without the need for ambient light and multiple cameras [11]. A unique benefit of RFID-based tracking is that it can allow simultaneous localization of large number of targets when combining digital IDs and locations together.

1.1 Prior arts and related works

Although passive tags can provide a distinguishable signal from ambient radio frequency (RF) reflections, accurate localization is still a very challenging task due to the rich scattering indoor environment. Among RFID localization methods, received signal strength (RSS) [1, 4, 31, 30] suffers from poor accuracy and reliability due to multi-path interference since RSS is not a sensitive function of distance. Time of flight (TOF) is not suitable for short range due to the synchronization difficulty, signal sampling complexity in capturing an ultra-wideband (UWB) wave packet in passive devices [5], and measurement of nano-second round-trip delay [13]. Carrier phase-based methods are preferred for their ultra-high sensitivity as a function of distance [3, 8].

In recent years, several phase-based systems had been proposed, such as holographic tag localization [14], Tagoram [6], RF-compass [10], PinIt [15], Backpos [12] and RF-IDraw [7]. However, these systems came with a variety of constraints

in order to be extended to a ubiquitous real-time 3D passive device localization system. These constraints include but are not limited to:

(1) Requirement of relative motion: Several systems have shown deca-centimeter to centimeter level accuracy but rely on relative reader and tag motion. Holographic RFID localization [14] and later Tagoram [6] utilized inverse synthetic aperture radar (ISAR) techniques [16] to form a large virtue antenna array in order to pin down the initial position of an RFID tag with a known trajectory. While PinIt [15] adopted an synthetic aperture radar (SAR) approach which required reader antenna motion in order to collect multi-path profiles of a target tag which was later compared to anchor tags. RF-compass [10] utilized a robot which carried several reference tags to rotate around a target tag to find its position. However, in many scenarios, the relative motion between tags and reader antennas cannot be satisfied. In some cases, the reader antennas position has to be fixed for indoor applications. Furthermore, when motion is required before localization, the system latency is usually high, making real-time applications more difficult.

(2) Availability of reference tags or anchor nodes: The localization accuracy can be greatly improved if we have the luxury of reference tags or anchor nodes with known accurate position. Both PinIt [15] and RF-compass [10] utilized reference tags. PinIt compared the multi-path profiles and found the nearest reference tag to the target tag. RF-compass relied on the distance comparison of the target tag to multiple reference tags to achieve a 2D-plane partitioning with the help of a moving robot. Reliance on reference or anchor tags brings forth the heavy dependence on the granularity of the reference tags. In order to achieve high accuracy, the number of required reference tags may be large. Reference tags also need initial deployment with accurate positions, which puts additional hurdles to many applications.

(3) Knowledge of moving trajectory: In order to mitigate multi-path effects, ISAR-based systems such as holographic RFID localization [14] and Tagoram [6] would need prior knowledge of the tag moving trajectory. Tagoram relaxed this constraint by fitting moving trajectory from tag moving speed estimation. However, not only the accuracy is compromised, but the latency is also long. The moving tag may need to finish the 10 laps of a fixed trajectory which took 5 minutes before localization can be achieved.

(4) Rigid configuration of reading antenna: Phase-based methods can be vulnerable to ambiguous phase cycles. Instead of directly determining the ambiguous cycle integer, systems like BackPos [12] constrained the tag motion within a region of "interrogation zone", where the differential distance from two reader antennas to the target tag falled within half wavelength. When the target tag was out of the interrogation zone, such system became unreliable. RF-IDraw [7] took advantage of antenna arrays with different resolutions and ambiguities in a 2D-plane. To resolve ambiguity, RF-IDraw required closely-spaced, low-resolution antenna arrays to remove the grating lobes. Furthermore, the rigid antenna configuration can be problematic to integrate with other system components.

(5) Limitation to 2D: Holographic RFID localization [14], RF-compass [10], Tagoram [6], BackPos [12] and RF-IDraw [7] were essentially 2D localization systems, and were difficult to extend to the 3D space. For example, RF-compass required a moving robot around the target tag which was difficult in 3D. BackPos and RF-IDraw utilized linear antenna arrays and hence difficult to resolve 3D positions. Holographic RFID localization and Tagoram needed to compute the image of "Hologram", which had high computational cost in the 3D space.

1.2 The indoor RF localization challenges

Can we build a real-time 3D indoor localization system for passive devices without the above constraints? First of all, we must understand the difficulties for the phase-based localization in the current RFID system. The main challenges include:

(1) The ambiguous phase cycles: Since the measured phase is always within $[0, 2\pi)$, cycle ambiguity exists when the distance is longer than one wavelength. When the measured phase is θ, the actual phase can be $\theta + 2n\pi$ where n is the cycle integer as depicted in Fig. 1(a). The cycle integer must be solved correctly in order to reduce ambiguity in the 3D location.

(2) Self-jamming and bandwidth limitation: For passive backscatter communication, the downlink and uplink are extremely asymmetric due to the need to reduce tag cost and complexity. Such an asymmetry brings the notorious jamming problem in RFID readers as shown in Fig. 1(b). It is not uncommon that the leakage from the reader transmitting signal to receiver is 80dB higher than the received tag response. Phase noise skirts of the strong transmitting signal at effective isotropic radiated power (EIRP) above 4 Watts can drastically raise the receiver noise floor [17, 18]. The input leakage signal needs proper isolation to be less than the 1-dB suppression point of the receiver to avoid saturation and nonlinear effects. The demanding high isolation from transmitter (Tx) to receiver (Rx) puts stringent requirements on frontend RF circulator and antenna reflection loss S_{11}, which leads to limited operation bandwidth due to the Bode-Fano criteria [19].

(3) Large phase error induced by multi-paths: A dense multi-path environment in Fig. 1(c) may cause measured phase error up to several tens of degrees. For example, if a multi-path component is only 3dB below the line of sight (LOS), the largest induced phase error is $\pm 45°$. We need to deal with low signal-to-interference ratio (SIR) even the LOS path appears to be clear. With moving scatterers such as human body, the phase detection can be easily smeared. The problem is even more complicated when the ambiguous cycle comes into play. Few works considered the theoretical phase error bound for correct phase cycle estimation.

1.3 Proposed approach

Notice that most of the previous attempts tackled the problem with commercial off-the-shelf (COTS) equipment and improved algorithms. In fact, the constrains come from not only the algorithm but also the hardware implementation. Hardware and software co-design approach may offer a better solution. In this paper, we propose a system to directly solve the above issues with high flexibility and least constraints. We offer an indoor real-time 3D localization approach for passive devices with centimeter level accuracy, small latency (0.155 seconds) and convenient calibration. The basic idea is to exploit nonlinear effects in passive devices instead of the conventional linear approach as shown in Fig. 2. When a passive tag receives a reader
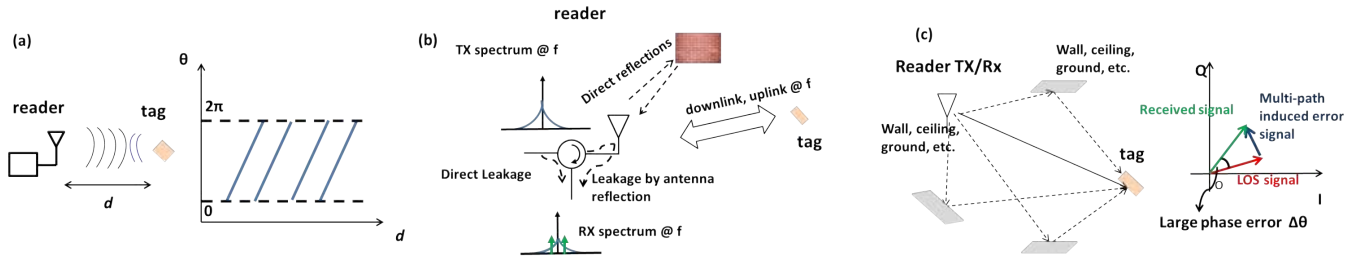
Figure 1: Challenges in phase-based localization: (a)Received phase of the backscatter signal is not a pure monotonic function of distance. Instead the phase has many ambiguous cycles.(b)Self-jamming problems in the conventional RFID system. Leakage signals and direct reflection from Tx to Rx can be over 80dB larger than the desired tag signal.(c)The dense indoor multi-path induces large phase error in the measurements.
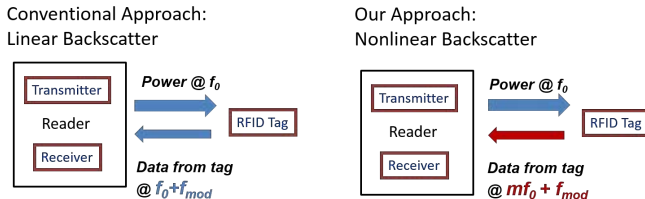

Figure 2: In the proposed nonlinear backscatter approach, a tag communicates to the reader at higher-order harmonics.

inquiry signal in the conventional backscatter, it responds to the reader by switching its antenna "on"and "off". The antenna switching effectively changes the reflected RF signal energy. Since the downlink and uplink are on the same carrier, the conventional backscatter is essentially linear. In our nonlinear backscatter approach, nonlinear circuit elements such as varactors and diodes are used to passively generate second or higher-order harmonics. The uplink information is then encoded on these harmonics instead of the fundamental carrier. The separation of downlink and uplink signals in nonlinear backscatter can fundamentally eliminate the self-jamming problem in conventional RFID, enabling broadband operation. The harmonic signal can be detected even if it is unmodulated. With the broadband operation, we then resolve ambiguous cycle integers with a sparse multi-frequency sequence which is selected by a heuristic optimization to offer the best phase error tolerance with small number of hopping frequencies. We compute 3D position efficiently by solving hyperboloid intersection using a fast nonlinear conjugate gradient (CG) search in a system setup with 4 Rx antennas and 1 Tx antenna.

1.4 Main contributions:

(1) To the best of our knowledge, we demonstrate the first 3D passive device localization system based on broadband nonlinear backscatter. Our proposed approach eliminates requirements on relative motions, deployment of anchor nodes and rigid antenna configuration, and is truly real-time.
(2) We show that extremely broadband backscatter operation in passive devices is feasible with nonlinear backscatter techniques. Broadband property is fundamentally important for ranging and localization applications. In conventional RFID system, operation bandwidth is limited by the self-jamming nature of linear backscatter communication. Previous works rarely attempted pursuing a broadband passive RFID operation.

(3) Our system is highly robust against multi-paths. With the help of broadband coherent carrier phase detection enabled by the nonlinear approach, we directly determine the phase cycle integer based on a heuristic multi-frequency continuous wave (HMFCW) ranging method [20]. We further generalize two basic theorems for HMFCW ranging regarding the phase error tolerance. Given the lowest frequency $f_{\min}$ and the highest frequency $f_{\max}$ in a continuous band that is available to use, the percentage bandwidth is defined as $BW\% = 2(f_{\max} - f_{\min})/(f_{\max} + f_{\min})$. HMFCW ranging is able to compute correct cycle integer with 100% accuracy when multi-path induced phase error is within $\pm 90° \times BW\%$. In our experiment, we show ranging error less than 1 cm with multi-path phase error that can go up to more than $\pm 60°$.
(4) The antenna configuration is flexible and only requires 4 Rx antennas to give a unique location in 3D space. The 3D location is directly computed from accurate ranging results with an efficient nonlinear CG algorithm to resolve the hyperboloid intersection problem.
(5) Our system requires minimal calibration efforts for the environment. The only calibration is to compute the cable delay between the receiving antennas and the reader.
(6) Our present system is real-time. The latency of our system to compute one 3D position presently is 0.155 seconds.

1.5 Paper organization

We will discuss the system overview in Sec. 2. The design on passive backscatter devices and the coherent receiver will be discussed in Sec. 3. We investigate the optimal selection of multi-frequency sequence to resolve phase cycle integer in Sec. 4. In Sec. 5, we present the 3D localization algorithm. In Sec. 6, we present experimental evaluation with our prototype system.

2. SYSTEM OVERVIEW

The proposed nonlinear backscatter localization system is shown in Fig. 3. The system consists of four main components: (1) Phase information acquisition; (2) Coherent phase detection; (3) Heuristic multi-frequency continuous-wave (HMFCW) ranging; (4) 3D position calculation.

The phase information acquisition component consists of 1 broadband Tx antenna at the fundamental frequency and 4 Rx antennas at the corresponding second harmonics. When the nonlinear tag has received the inquiry signal from the Tx antenna, it responds to the 4 Rx antennas by re-radiating the second harmonic signals. We later compute the differential distance from the tag to different Rx antennas in order to pin down its accurate position.
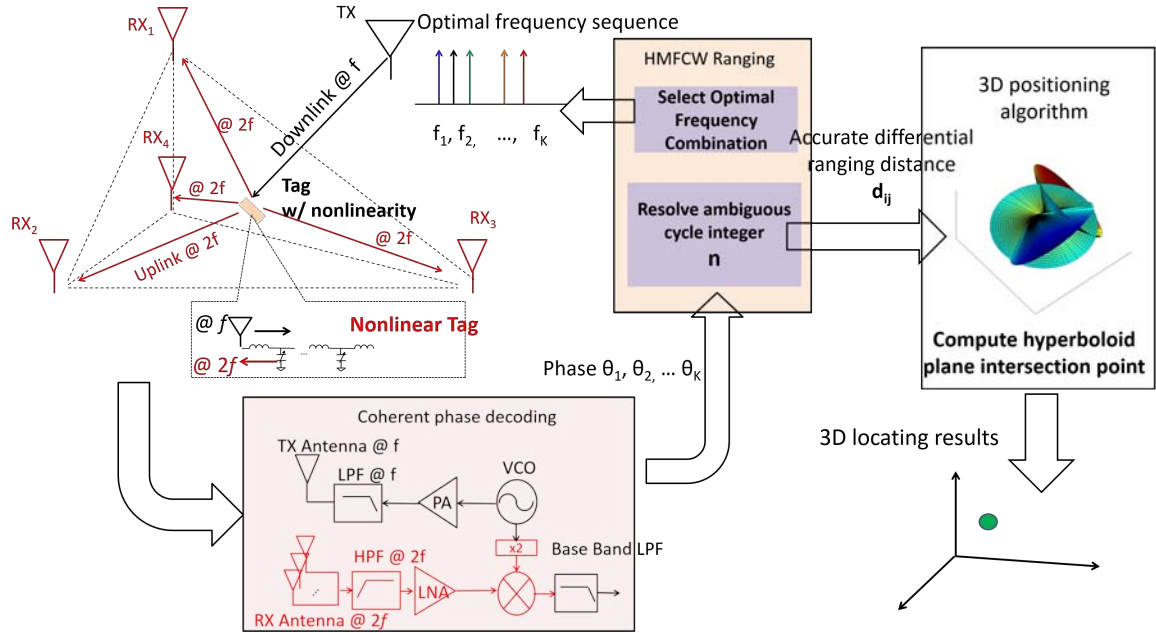
Figure 3: Illustration of the nonlinear backscatter 3D localization system.

The phase detection component utilizes a homodyne receiver to directly covert the backscatter harmonic signal to baseband and compute the the carrier phase. One unique advantage of RFID localization is coherent detection without carrier offset between the Tx and Rx signals. This remains true when we use nonlinear backscatter for the round trip. Because the uplink harmonic signal is passively generated on tags, we are able to coherently detect the carrier phase by utilizing harmonics generated in the Tx chain.

The HMFCW ranging component has two functions. It first decides what frequencies are transmitted based on the available bandwidth. The transmitting frequency sequence is very important to resolve the ambiguous phase cycle integers reliably in HMFCW ranging. After receiving the decoded harmonic carrier phase, the cycle integer for each frequency is calculated. The final output is the differential distance from the tag to the pair of Rx receiving antennas.

The last component is the 3D position computation. Each differential distance d_{ij} determines a hyperboloid in the 3D space. In order to uniquely determine the 3D position, we need to compute the intersection point of at least 3 hyperboloids. We convert such a task into an optimization problem and utilize the efficient nonlinear CG search.

3. SELF-JAMMING ELIMINATION

3.1 Understanding present limitations

In order to achieve accurate ranging, broad bandwidth can help tolerate multi-path phase errors. Such trade-off has been exploited in frequency modulated continuous-wave (FMCW) radar and UWB systems [21], which is however very challenging in conventional backscatter communication. The major problem is that passive tags are battery-less and hence they cannot afford an RF frontend to generate or amplify an RF signal in the range of GHz. Today, the RFID tag operating power is typically in the vicinity of 10 μW. Since a tag passively reflects the reader inquiry signal, the power of the received tag response P_r at the reader experiences twice free-space propagation losses, one from the downlink

and the other from the uplink:

$$P_r = GP_t \frac{\lambda^4}{(4\pi)^4|\mathbf{r}_{tag} - \mathbf{r}_{reader}|^4} \quad (1)$$

where G includes reader Tx/Rx antenna gains and tag Tx/Rx antennas gains, $\mathbf{r}_{tag}$ and $\mathbf{r}_{reader}$ are position vectors of the phase center of tag and reader antennas, P_t is the reader transmitting power and λ is the wavelength. Notice that P_r is inversely proportional to the distance to the 4th power.

Backscatter communication also requires a very strong reader inquiry signal to power up the passive tag. So, today, an RFID reader usually operates with $> 1\,W$ transmitting power while P_r can be less than 100 dB of the Tx power.

This brings forth the problem of self-jamming. The RF signal flow of a conventional RFID reader is shown in Fig. 4. In addition to P_r, there are two main leakage signals. One leakage path is from the circulator [19] (denoted as path 1 in Fig. 4). A circulator is an isolation device that is commonly used to separate the Tx/Rx channels. A good RF circulator can usually provide 25 to 30dB isolation. The other leakage path is from the front end antenna reflection and is heavily dependent on antenna reflection loss (S_{11}) (denoted as path 2 in Fig. 4). Let S_t denote the transmitted signal, then the total leakage signal S_{leak} can be written as

$$S_{leak} = S_{11}^{ant}S_t + \rho S_t \quad (2)$$

where the antenna reflection is represented by S_{11}^{ant} and the isolation of circulator is denoted as ρ. The received signal is the sum of the leakage signals and the tag response, which is fed into the input of the receiving block. If the leakage signal is not well suppressed, it may cause receiving saturation which leads to failure of operation. Another issue with unsuppressed leakage is the raised noise floor. Different from other communication systems, passive backscatter is usually full duplex in the way that the Tx and Rx are active simultaneously. The noise floor is set by the phase noise of the leakage signal rather than the thermal noise floor. The phase noise [22] is a low-frequency noise located around the carrier

and is very difficult to filter out. Phase noise filtering would require ultra high Q components that are not commonly available in RF frequency. Fig. 5 shows the Leeson's model [22] of phase noise. When the offset frequency approaches zero, the noise power spectrum will increase according to $1/\Delta f^2$. The noise slope may be even $1/\Delta f^3$ when the offset frequency further decreases. For passive devices, because the operating power is very low, hence the data modulation is at the range of kHz to hundreds of kHz. The modulated backscatter signal will overlap with the phase noise of the leakage signal. For a common RF frequency source, the phase noise at 10 kHz is about -80 dBc/Hz. If a leakage signal is of 0 dBm, this -80 dBm/Hz phase noise floor is much higher than the -174 dBm/Hz thermal noise floor. For an even larger leakage, the desired backscatter may be totally buried in the phase noise skirt as depicted in Fig. 5.

Due to the above reasons, the leakage signal must be handled properly which will in turn severely limits the ability of a broadband operation. As shown in Fig. 6, the front-end antenna reflection loss S_{11} must be minimized for all operating frequencies. However, there is a trade-off between the reflection loss and bandwidth for RF antennas, which is called the Bode-Fano criteria [19, 22]. If we want broad bandwidth, we have to sacrifice the lowest S_{11}, which is intolerable in today's RFID receiver. For an RC load, the Bode-Fano criteria can written as:

$$\int_0^\infty \ln \frac{1}{|S_{11}(\omega)|} d\omega \leq \frac{\pi}{RC} \qquad (3)$$

Please note that the problem in reality is much more complicated than shown in Eq. (3). Practical antennas also contain inductive elements and the input impedance can vary dramatically as frequency changes. Therefore, a present RFID reader can only have receiving sensitivity of around -70 dBm [23] with very limited bandwidth of operation.
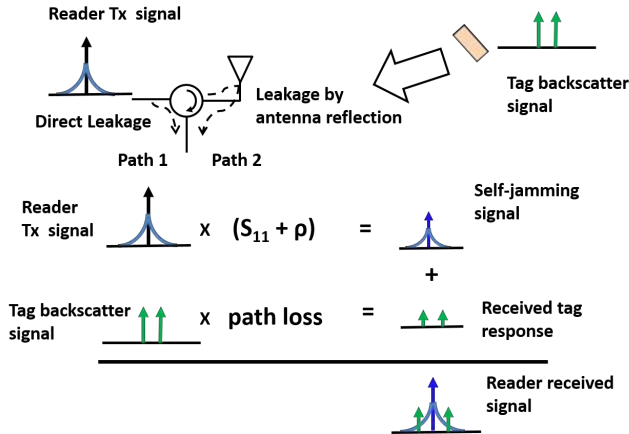

Figure 4: Leakage signals and received backscatter signal in a conventional RFID reader.

3.2 Nonlinear backscatter techniques to enable broadband harmonic backscatter operation

The self-jamming problem can be fundamentally eliminated via nonlinear backscatter, enabling broadband operation, as shown in Fig. 7. When we modulate the uplink
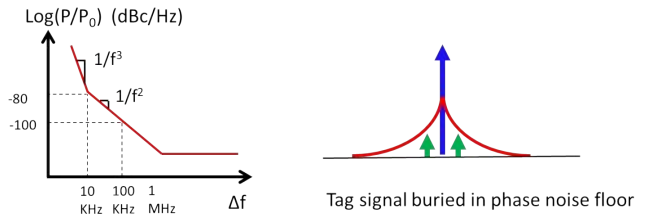

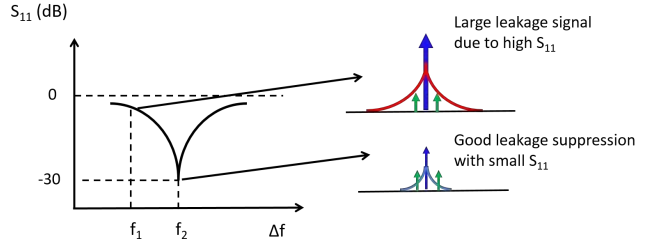Figure 5: Leeson's phase noise model and the noise floor raised up in a conventional RFID reader.

Figure 6: Large leakage signals caused by large antenna reflection S_{11} and hence bandwidth limited in a conventional RFID reader.
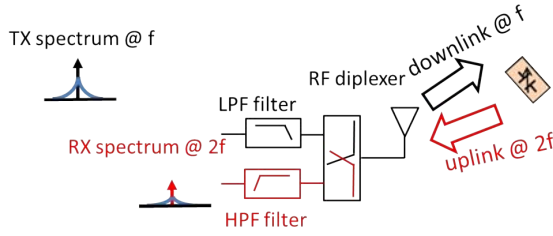
on second harmonic which is passively generated by nonlinear devices, we can use broadband low-pass filters (LPF) and high-pass filters (HPF) to easily separate the Tx and Rx signals. Due to the large frequency separation, it is not difficult to filter out the Tx signal at the fundamental frequency by 90 dB. The nonlinear backscatter approach is very flexible in construction and deployment. An RF diplexer can be inserted between the antenna and the filter banks. In comparison with the conventional RFID reader, where monostatic antenna with a circulator is more stable, our nonlinear backscatter method can readily implement the multi-static tranceiver approach as shown in Fig. 7, because antenna isolation by filters in close space can now be guaranteed.

In nonlinear backscatter, the antenna reflection loss S_{11} is not a bottleneck any more, so broadband tranceiver design is much easier. Since all the harmonics from power amplifier (PA) is immediately stopped by the LPF filter, only the fundamental frequency is at the Tx antenna. Therefore, no matter how much power at the fundamental frequency is reflected from the antenna to the receiving input, it can be immediately stopped by the HPF. The noise floor for the receiver is determined by the thermal noise floor at -174 dBm/Hz and now we can even retrieve the phase of un-modulated carriers.

3.2.1 Broadband nonlinear tag design

Previous research on distributed microwave structures had shown that higher-order harmonics can be efficiently generated with periodically loaded varactors and inductors [24, 25, 41]. Such microwave structures are called nonlinear transmission lines (NLTLs) [26], which allow ready broadband matching to the antenna. As shown in Fig. 8(a) for a typical section of NLTL, when the fundamental frequency propagates along NLTL, due to the nonlinearity of varactors, second and higher-order harmonics are generated in each section. When the propagation speed of harmonics is equal to that of the fundamental frequency, they will add up constructively with the harmonics generated in later sec-
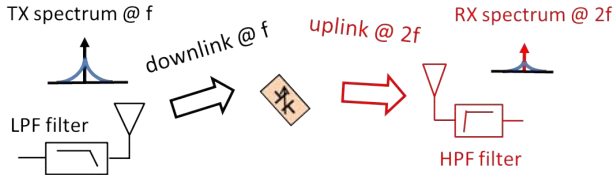
Figure 7: **Nonlinear backscatter based on passive second harmonic generation with mono-static and multi-static tranceivers.**
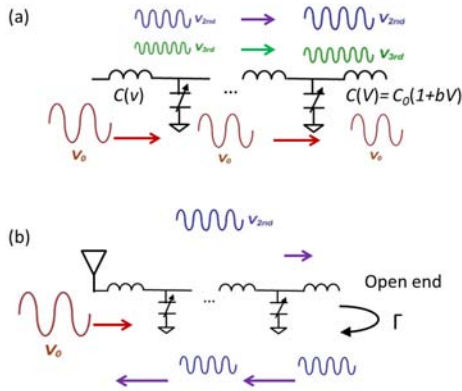

Figure 8: **(a) Harmonic generation in NLTL due to the nonlinearity of varactors.(b) Reflective NLTL with the open end for single-antenna configuration.**

tions. Hence, the power in the fundamental frequency will be gradually converted to harmonics. Because the tag received signal is usually below 0 dBm, it can be treated as a small signal. The varactor can then be treated as a variable capacitor whose capacitance is a function of the voltage using Taylor expansion to the first order [25]:

$$C(V) = C_0(1 + bV) \qquad (4)$$

where C_0 is the capacitance corresponding to zero voltage and the slope b reflects the nonlinearity which is process dependent. For a common RF CMOS process, b is about 0.5/V. The second harmonic at different stages can be written as [24, 25]:

$$|V_{2nd}(x)| = \left| \frac{bV_0^2}{2} \frac{\gamma_2^2}{\gamma_2 + 2\gamma_1} \frac{\sinh(\frac{\gamma_2 - 2\gamma_1}{2}x)}{\gamma_2 - 2\gamma_1} e^{-\frac{\gamma_2 + 2\gamma_1}{2}x} \right| \qquad (5)$$

In Eq. (5), x is the stage number and $\gamma_{1,2}$ are propagation constants for fundamental and second harmonic signals including the dispersion and loss effects. An efficient design would require careful trade-offs between the number of stages, dispersion and loss effects [24].

3.2.2 Reflective NLTL with a single antenna

In order to use a single-antenna configuration, we adopt a reflective structure as depicted in Fig. 8(b). We terminate one terminal of NLTL with an open end [41] and the other terminal with a broadband antenna that covers both fundamental and second harmonic bands. The signal propagates to the end of NLTL and is reflected by the open circuit with a reflection coefficient $\Gamma = 1$. The reflected signal then propagates back towards the tag antenna for backscatter.

3.2.3 Integration NLTL with an RFID circuitry

We can integrate the NLTL with a normal RFID circuitry. An RFID system consists of a power harvesting unit, a digital control unit and memory logic. When the uplink is modulated on the second harmonic, we need a switch to control the signal flow in NLTL. At the same time, to allow efficient power harvesting to wake up the tag, no power should be spent on harmonic generation during the start-up state. We can achieve the above purposes by adopting a power routing strategy.

We show a design example with the assistance of openplatform WISP [27] for the tag logic circuits. The photo is shown in Fig. 9(a) with the block diagram in Fig. 9(b). We integrate the WISP tag with NLTL by adding the power routing unit in the frontend. The power routing unit, which is used to connect to an antenna to receive signals from the reader, consists of a quarter-wavelength ($\lambda/4$) 50 Ω meandering micro-strip line, and two RF switches. In the startup/energy-harvesting mode, both Switch A and Switch B are set to "off" without the generated power supply, thus blocking power into NLTL. The energy-harvesting module is matched to 50 Ω and the antenna matching remains after the $\lambda/4$ microstrip line so all power is directed to energy harvesting. In the harmonic generation mode, both Switches A and B are pulled to the "on" state. The drain node on Switch A is grounded, and the $\lambda/4$ line acts as an impedance transformer so that a large impedance appears at the input end. Meanwhile, Switch B is also "on" and the characteristic impedance looking into NLTL is matched at 50 Ω, so all of the received power is routed to generate second harmonics efficiently. Fig. 9(c) shows the measured tag sensitivity. The reflective output second harmonic power at 0 dBm input is shown in Fig. 9(d).

3.2.4 The harmonic reader implementation for broadband operation

With nonlinear backscatter, we can build a reader with broad operation bandwidth. Fig. 9(e)(f) show the homodyne reader photo and block diagram. Besides the Tx/Rx signal separation block which is illustrated in Fig. 7, the reader supports 1 Tx antenna and 4 Rx antennas for 3D localization as shown in Fig. 3. The received harmonic signal is directly converted to the baseband and sampled by the analog-to-digital converter (ADC) on the Cortex M4 STM 32-bit micro-controller. To allow coherent phase detection, the local oscillator (LO) signal to the mixer is coupled from harmonics of the power amplifier in Tx. The reader employs variable gain amplification in both Tx and Rx to enhance the dynamic range. Our reader communicates to a host computer by Bluetooth. Fig. 9(g) shows the measured maximum Rx gain of our reader, which achieves 60 dB gain from 1400 MHz to 2400 MHz for received harmonic signals. The measured Tx output power is 29 dBm from
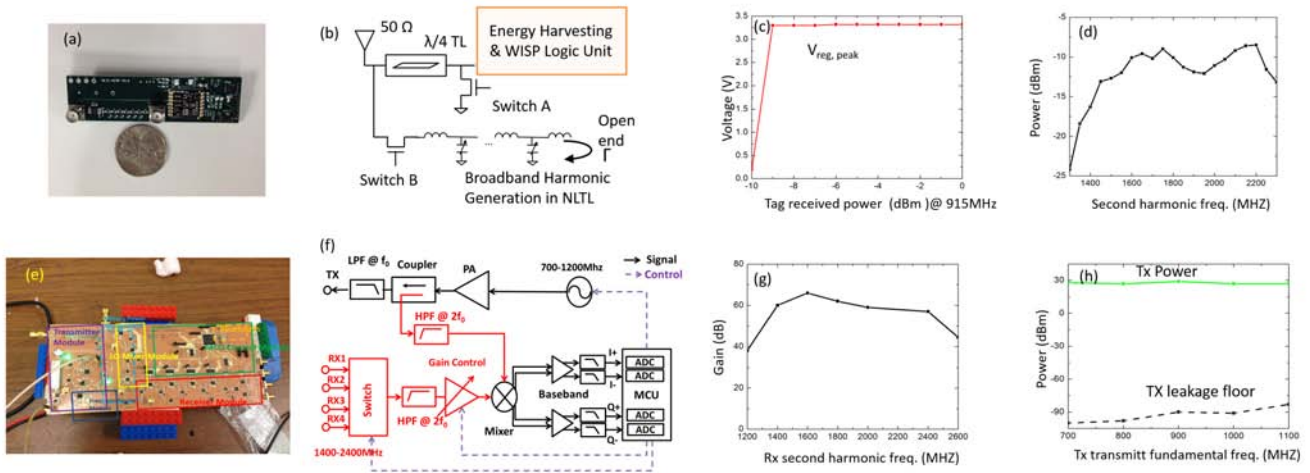
Figure 9: (a) Photo of a passive nonlinear tag integrated with WISP logic. **(b)** Block diagram of the proposed passive nonlinear tag. **(c)** Measured tag sensitivity. **(d)** Measured output second harmonic from reflective NLTL with 0dBm fundamental input power. **(e)** Photo of the proposed homedyne nonlinear backscatter reader. **(f)** Block diagram of the reader. **(g)** Measured reader RX receiving gain in broadband. **(h)** Measured maximum reader TX power and corresponding input referred interference in broadband.

700 MHz to 1100 MHz as shown in Fig. 9(h). When Tx is at maximum power, the measured interference signal to the receiving chain is also plotted in Fig. 9(h), which is below -90 dBm. The interference can be further suppressed with software cancellation [45]. With the implemented reader, we can pursue a broadband operation over 45% bandwidth.

4. HMFCW RANGING ALGORITHM

A phase-based ranging algorithm needs to accurately resolve ambiguous phase cycle integers with maximum tolerance of phase errors. Traditional multi-frequency ranging based on the Chinese Remainder Theorem (CRT) showed that frequency redundancy can help removing ambiguity [28]. However, CRT-based methods are vulnerable under multi-path phase errors and cannot provide a theoretical phase error bound for correct phase cycle integer estimation. In this work, we adopt heuristic optimized continuous-wave (HMFCW) ranging which was proposed in [20]. We further generalize two theorems for HMFCW ranging. The two theorems show that in order to tolerate large phase error while solving phase cycle integers correctly, we can rely on optimal utilization of the broad bandwidth which is enabled by our nonlinear backscatter tag and reader design discussed in Sec. 3.

Assume Tx is at the fundamental frequency f_k, the correspondingly measured phase of second harmonic backscatter signal is $\theta_k \in [0, 2\pi)$. The distance from tag to i-th antenna is d_i and the differential distance d_{ij} is

$$d_{ij} = d_i - d_j \qquad (6)$$

Then there is an ambiguous cycle integer n_k for measurements on the k-th frequency which gives

$$d_{ij}^{(k)} = \frac{\theta_k}{2\pi} \frac{\lambda_k}{2} + n_k \frac{\lambda_k}{2} \qquad (7)$$

where $\lambda_k = c/f_k$ is the wavelength with c equal to the speed of light. Our goal is to correctly computes n_k within a reading range R, where

$$-R/2 < d_{ij} \le R/2 \qquad (8)$$

Typical R for indoor localization is in the range of several meters.

4.1 Error tolerance function

The difficult problem is the large phase error in indoor environment. HMFCW ranging is much more robust than those based on CRT. In HMFCW ranging, a reader transmits a sequence of K frequencies $\mathbf{f} = (f_1, f_2, \cdots, f_K)$ and HMFCW ranging first defines the **error tolerance** as a function of $\mathbf{f}$ and the reading range R.

Definition 1. Let $\lambda_k = c/f_k$, the error tolerance function is defined as

$$T(\mathbf{f}, R) = \min_{\mathbf{b}=(b_1,\cdots,b_K)} \max_{1 \le k,l \le K} \pi \frac{|\lambda_k b_k - \lambda_l b_l|}{\lambda_k + \lambda_l}$$
$$s.t. \begin{cases} b_k \in \mathbf{Z}, & 1 \le k \le K & \sum_k b_k^2 > 0 \\ \frac{1}{2}|\lambda_k b_k| < R + \frac{1}{2}\lambda_k \end{cases} \qquad (9)$$

THEOREM 1. *Let $\Delta\theta_k$ denote the measured phase error for the k-th second harmonic frequency and $-\Delta\theta_{max} \le \Delta\theta_k \le \Delta\theta_{max}$. The measured phase $\theta_k = \theta_k^{ideal} + \Delta\theta_k$, where θ_k^{ideal} is the "ideal" phase when there is no multi-path error. If*

$$\Delta\theta_{max} < T(\mathbf{f}, R) \qquad (10)$$

then we can resolve cycle integers $\mathbf{n} = (n_1, n_2, \cdots, n_K)$ correctly by finding the integer vector $\mathbf{n}$ that satisfies

$$-R - \lambda_k < n_k \lambda_k \le R \quad \forall k \qquad (11)$$

and

$$\frac{2\pi |n_k \lambda_k + \frac{\theta_k}{2\pi}\lambda_k - n_l\lambda_l - \frac{\theta_l}{2\pi}\lambda_l|}{\lambda_k + \lambda_l} < T(\mathbf{f}, R) \quad \forall k,l \qquad (12)$$

PROOF. Assume the actual distance is d which is also the distance for θ_k^{ideal}. At the k-th frequency, we have phase error $\Delta\theta_k$, so the measured distance $d^{(k)}$ for the k-th frequency is

$$d^{(k)} = d + \frac{\Delta\theta_k}{2\pi} \frac{\lambda_k}{2} = \frac{n_k\lambda_k}{2} + \frac{\theta_k}{2\pi} \frac{\lambda_k}{2} \qquad (13)$$

where $\mathbf{n} = (n_1, \cdots, n_k, \cdots, n_K)$, $k \in \{1, \cdots, K\}$ are the true integers that we want to know. Because of Eq. (8), we have

$$-\frac{R}{2} < \frac{n_k \lambda_k}{2} + \frac{\theta_k}{2\pi} \frac{\lambda_k}{2} \leq \frac{R}{2} \quad (14)$$

and $0 \leq \theta_k < 2\pi$. Hence n_k satisfies Eq. (11). Also because of Eq. (13), we have

$$|d^{(k)} - d^{(l)}| = |\frac{\Delta\theta_k}{2\pi} \frac{\lambda_k}{2} - \frac{\Delta\theta_l}{2\pi} \frac{\lambda_l}{2}| < \frac{\Delta\theta_{\max}}{2\pi} \frac{\lambda_k + \lambda_l}{2} \quad (15)$$

By using Eqs. (10) and (13), we know n_k and n_l where $k, l \in \{1, \cdots, K\}$ satisfy Eq. (12) and hence the true $\mathbf{n}$ is a solution that satisfies the condition in Eqs. (11) and (12).

Next, we will prove that $\mathbf{n}$ is the unique solution by contradiction. Suppose there is another solution $\tilde{\mathbf{n}} = \mathbf{n} + \mathbf{b}$. Since both $\mathbf{n}$ and $\tilde{\mathbf{n}}$ satisfy Eq. (11), integer b_k must satisfy $\frac{1}{2}|\lambda_k b_k| < R + \frac{1}{2}\lambda_k$ and because $\tilde{\mathbf{n}} \neq \mathbf{n}$, $\sum b_k^2 > 0$. Since both $\mathbf{n}$ and $\tilde{\mathbf{n}}$ satisfies Eq. (12), this leads to:

$$\frac{\pi|b_k \lambda_k - b_l \lambda_l|}{\lambda_k + \lambda_l} < T(\mathbf{f}, R) \quad \text{for} \quad \forall\, 1 \leq k, l \leq K \quad (16)$$

Eq. (16) contradicts with the definition of $T(\mathbf{f}, R)$ in Eq. (9). Therefore, the desired integer $\mathbf{n}$ is the unique solution that satisfies condition in Eqs. (11) and (12). $\quad\square$
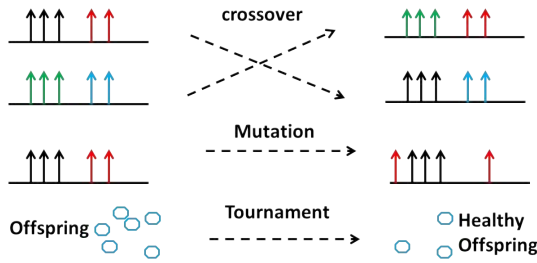

Figure 10: Selecting optimal frequency combination via a genetic algorithm.

4.2 Selecting optimal frequency combination

As long as the measured phase error is smaller than $T(\mathbf{f}, R)$ in Eq. (10), we can always resolve cycle integers correctly. We now need to select a frequency combination that can maximize the error tolerance function $T(\mathbf{f}, R)$. The maximum value of $T(\mathbf{f}, R)$ is defined as the **phase error threshold** Φ:

Definition 2. The phase error threshold:

$$\Phi(\mathbf{F}, K, R) = \max_{\mathbf{f} = (f_1, \cdots, f_K)} T(\mathbf{f}, R) \quad (17)$$

where $\mathbf{F}$ represents the bandwidth of operation and K is the number of frequencies used for ranging. Assume $f_{\max} = \max\{f, f \in \mathbf{F}\}$ and $f_{\min} = \min\{f, f \in \mathbf{F}\}$ are the maximum and minimum frequencies in $\mathbf{F}$, We define the percentage bandwidth as $\text{BW\%} = 2(f_{\max} - f_{\min})/(f_{\max} + f_{\min})$.

THEOREM 2. *An integer $K(\mathbf{F}, R)$ exists for a continuous frequency band $\mathbf{F}$ with $BW\% < 100\%$ and a reading range R so that for $K > K(\mathbf{F}, R)$, an optimal frequency combination $\mathbf{f}^{opt} = (f_1^{opt}, f_2^{opt}, \cdots, f_K^{opt})$ can be found for which*

$$\Phi(\mathbf{F}, K, R_{max}) = T(\mathbf{f}^{opt}, R) = 90° \times BW\% \quad (18)$$

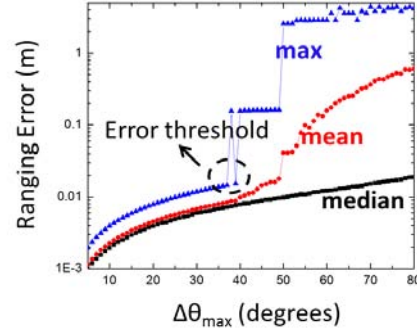**Figure 11: Ranging error from Monte Carlo simulation using frequencies shown in Table.1.**

PROOF. First note that

$$T(\mathbf{f}, R) \leq \min_{\mathbf{b} = (1, \cdots, 1)} \max_{1 \leq k, l \leq K} \pi \frac{|\lambda_k b_k - \lambda_l b_l|}{\lambda_k + \lambda_l}$$
$$\leq \pi \frac{\lambda_{max} - \lambda_{min}}{\lambda_{max} + \lambda_{min}} = 90° \times \text{BW\%} \quad (19)$$

so we only need to prove that the upper bound is attainable. Consider a special frequency combination

$$f_k = f_{\max} \left(\frac{f_{\min}}{f_{\max}} \right)^{\frac{k-1}{K-1}} \quad 1 \leq k \leq K \quad (20)$$

Let $M = \lceil \frac{2R}{\lambda_{\min}} \rceil + 1$, as long as

$$K > \left\lceil \log_{\frac{M+1-0.5\text{BW\%}}{M+0.5\text{BW\%}}} \left(\frac{1 + 0.5\text{BW\%}}{1 - 0.5\text{BW\%}} \right) \right\rceil + 1 \quad (21)$$

It can be shown that with $\text{BW\%} < 100\%$, $T(f, R) = 90° \times \text{BW\%}$. $\quad\square$

Theorem 2 dictates that we can always find an optimal frequency combination in a continuous frequency band so that our error tolerance is maximized. The maximum error toleration is equal to $\text{BW\%} \times 90°$. The larger the bandwidth we have, the more robust we are to the multi-path induced phase error. For example, if we have a system with $\text{BW\%} = 50\%$, we can tolerance phase error from $-45°$ to $45°$ with 100% reliable cycle integer calculation. Although Eq. (20) gives an optimal solution, however, it is pessimistic when considering the number of frequency required to meet the upper bound. Usually, the upper bound can be achieved with less than 6 frequencies for $R = 4m$ and $\text{BW\%} = 30\%$.

A heuristic optimization program can be employed to find the optimal frequency combination with small number of frequencies. In our case, we choose the genetic algorithm (GA) which utilizes three mechanisms: crossover, mutation and tournament. At the start, we randomly select a poll of frequency combinations. Then these frequency vectors mate with each other to produce offspring with a mutation probability. The next generation is then generated by selecting healthy offsprings by comparing the cost function $T(\mathbf{f}, R)$ through a tournament. This process is briefly illustrated in Fig. 10. After pinning down the optimal frequency combination, ranging can be performed using Algorithm 1.

In this work, we pick optimal frequency combinations shown in Table. 1. Frequency combination #1 achieves phase error threshold of $34°$ and Fig. 11 shows the simulated ranging results for median, mean and max errors for a reading ranging

of 4 meters. The phase error for each frequency is uniformly distributed within $[-\Delta\theta_{\max}, \Delta\theta_{\max}]$. We can achieve median ranging error below 1 cm even under $\Delta\theta_{max} = 50°$.

Algorithm 1 HMFCW ranging with optimal frequency combination

Inputs: wavelength for **optimal** frequency combination $\lambda_1 > \lambda_2 > \cdots > \lambda_K$, measured phase $(\theta_1, \theta_2, \cdots, \theta_K)$, reading range R

Outputs: distance d

1: $\Phi = 2\dfrac{\lambda_1 - \lambda_K}{\lambda_1 + \lambda_k}\dfrac{\pi}{2}$ ▷ compute phase error threshold

2: $N_{\max} = \dfrac{R}{\lambda_K} + 1$ ▷ compute the range of cycle integer for λ_K

3: **while** Iter $\leq$ MaxIter **do**

4:      **for** $n_K = -N_{\max} \rightarrow N_{\max}$ **do**

5:          $d_{\text{temp}} = n_K\dfrac{\lambda_K}{2} + \dfrac{\theta_K}{2\pi}\dfrac{\lambda_K}{2}$

6:          **for** $i = 1 \rightarrow K - 1$ **do**

7:              $n_i = round\left(\dfrac{d_{temp} - \frac{\theta_i}{2\pi}\frac{\lambda_i}{2}}{\frac{\lambda_i}{2}}\right)$

8:          **end for**

9:      **end for**

10:      **if** $\dfrac{\pi|n_i\lambda_i + \frac{\theta_i}{2\pi}\lambda_i - n_j\lambda_j - \frac{\theta_j}{2\pi}\lambda_j|}{\lambda_i + \lambda_j} < \dfrac{\Phi}{2}$ for $\forall i, j$ **then**

11:          Break   ▷ solution found

12:      **end if**

13:      $\Phi = \tau\Phi$ ▷ if no solution found, relax phase error threshold

14: **end while**

15: $d = \dfrac{1}{K}\displaystyle\sum_{i=1}^{K}\left(\dfrac{\lambda_i}{2}n_i + \dfrac{\theta_i}{2\pi}\dfrac{\lambda_i}{2}\right)$ ▷ compute average

---

5. 3D LOCALIZATION ALGORITHM

In the previous sections, we have discussed the robust and accurate 1D ranging. Since each ranging result is a differential distance from a tag to two antennas at different position, in 3D space, one differential distance measurement gives a hyperboloid as shown in Fig. 12(a). To uniquely pin down a 3D tag position, at least three hyperboloids are required to compute the intersection point as depicted in Fig. 12(b). We achieve such task by solving the following optimization problem:
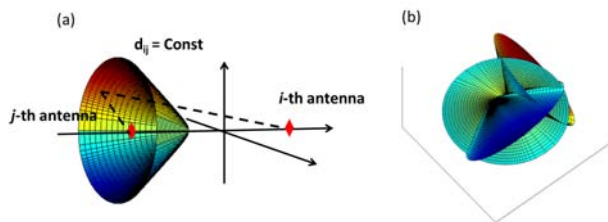

Figure 12: 3D localization by hyperboloid intersection.

$$\min_{\mathbf{p}} \sum_{i=2}^{4}\left(|\mathbf{p} - \mathbf{p}_1^{\text{ant}}| - |\mathbf{p} - \mathbf{p}_i^{\text{ant}}| - d_{1i}\right)^2 \qquad (22)$$

where the target tag position is denoted as $\mathbf{p} = (x, y, z)$ and the i-th antenna position is p_i^{ant}. The problem is essentially a nonlinear optimization problem. We solve it efficiently with the Fletcher-Reeves nonlinear conjugate gradient (CG) method [44]. Fletcher-Reeves nonlinear CG can be trapped
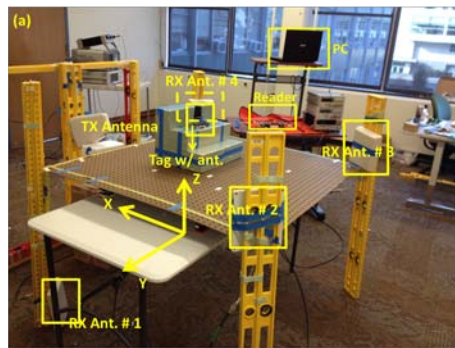

Figure 13: Experimental setup in indoor environments: (a) An open Lab; (b) A narrow lounge; (c) A classroom.

with local minima. To avoid such a problem, we select the initial point $\mathbf{p}_0$ from a poll of 300 randomly generated initial points for a comprehensive search.

For 3D localization, there are two main error sources. The first error source comes from the ranging measurement error while the second error is from the uncertainty in the phase center position of the 4 Rx antennas [32]. In this work, since we can directly resolve the ambiguous phase cycle integer even under large phase error, the ranging error is typically in the range of millimeter level. The major localization error is contributed from the antenna phase center uncertainties under broadband which is typically about ± 3 cm [32]. Notice that the phase center uncertainty will impact the precision against the ground truth, but will not change the measurement consistency.

6. EXPERIMENTAL EVALUATION

We evaluate the the proposed approach through intensive experimental measurements in indoor environments as shown in Fig. 13. We will present final 3D localization results as well as the 1D ranging and 2D localization. The transmitting frequency combination used in the 1D, 2D and 3D evaluations is the #1 sequence shown in Table. 1. The #2 sequence with reduced number of frequencies is used for the real-time tracking evaluations.

Hardware: The harmonic reader and the tag were implemented on PCB and are shown in Fig. 9(a)(e). The PCB tag was connected to a single antenna (Tagolas broadband antenna [33]) with average gain of -1.9 dBi. For continuous tracking, we adopted broadband whip antenna [34] for its reduced size. As the WISP was designed based on general-purpose micro-controller platform, which was power hungry and less efficient in energy harvesting compared to ASIC RFID tags. To avoid interruption in the operation continuity due to energy harvesting inefficiency of the present prototype, we bypassed the digital logics when performing continuous real-time tracking. For 3D localization, 4 Rx patch antennas which covered the harmonic band and 1 Tx

Table 1: Optimal Tx frequency combinations used in experiment

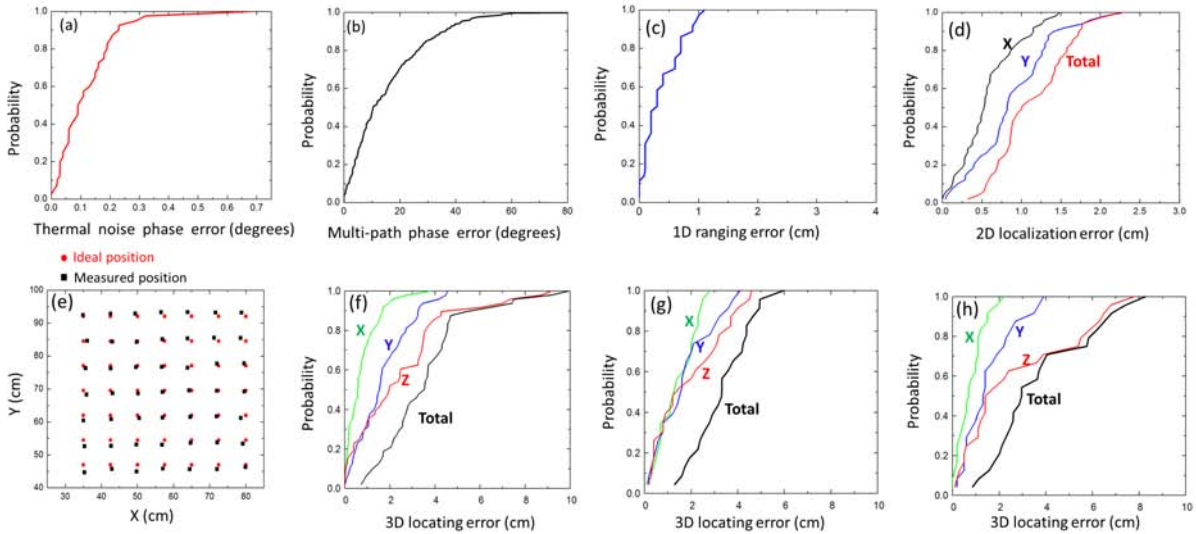| #	No.of freq.	Freq. (MHz)	BW%	Phase error threshold Φ	Reading range R
1	8	721 750 829 889 950 996 1045 1060	38%	34°	4 m
2	5	829 889 950 1033 1080	26%	24°	4 m

Figure 14: (a) Measured CDF of thermal noise induced phase error. (b) Measured CDF of multi-path induced phase error. (c) Measured CDF of 1-D ranging error. (d) Measured CDF of 2-D localization error. (e) A sample of 2D location measurements. (f)(g)(h) Measured CDF of 3D localization error in environments shown in Fig. 13 (a),(b) and (c), respectively.

Yagi antenna which covered the fundamental frequency band were used. To help measure the localization error, we set up a wooden table with ruler markers. The 4 Rx antenna positions were $(122, 124, -83)$ cm, $(12, 124, 0)$ cm, $(12, 14, 0)$ cm, $(122, 14, 0)$ cm, respectively. The distance from the Tx antenna to the center of the table was 100 cm. The reader communicated to the host computer through Bluetooth.

Software: The control program on the host computer was implemented via National Instrument Labview. After obtaining data from reader via Bluetooth, Labview will then call the ranging and localization programs. A STM32 Cortex M4 micro-controller coordinated amplification for both transmitter and receiver, the frequency synthesizer which handled frequency hopping, the ADC sampling for the decoded phase values, and communication between the host computer and the reader. The control program on the micro-controller was implemented with the Chibi-OS RT platform.

6.1 1D ranging measurements

The cumulative distribution function (CDF) of thermal-noise induced phase measurement error and the multi-path induced phase measurement error in an open lab are shown in Fig. 14(a)(b). The thermal induced phase error is below $1°$, while error is dominated by multi-path phase error which can be as large as $60°$. However, our system can tolerate such large phase error by reliably computing phase cycle integers within a search range of $R = 4$ m. The CDF of 1-D ranging is shown in Fig. 14(c). We achieve ranging below 1 cm over 90% with median error of 3 mm.

6.2 2D localization measurements

The CDF of 2D measurement results is shown in Fig. 14(d).

In 2D experiments the #1 Rx antenna position was mounted at $(122, 124, 0)$ cm and the rest 3 Rx antenna positions remained unchanged. The search space is constrained to 2D. We achieved median error of 0.53 cm and 0.82 cm in the X and Y positions respectively. A sample measurement in the 2D plane is shown in Fig. 14(e), where we put the tag on the lattice in random order and our system was able to compute each location instantly.

6.3 3D localization measurements

The CDF of 3D localization measurements are shown in Fig. 14(f)(g)(h). Three scenarios shown in Fig. 13 were tested to demonstrate robust measurements under different indoor multi-path interferences. The measurement was conducted in a region of 60 $cm \times$ 60 $cm \times$ 40 cm above the table with the help of a foam stair which was put at different locations on the table. For lab environment, we achieved median errors of 0.59, 1.54 and 1.97 cm for X, Y and Z coordinates and a total median error of 3.5 cm. While the maximum errors for X, Y, Z are 3.82, 4.56 and 9.17 cm. By comparing Fig. 14(g)(h) to Fig. 14(f), the measurements were shown to be stable in other indoor environments. The major contribution of the measurement error is from the measured Rx antenna position error. Because of the low diversity in the Z direction as we mounted Rx antenna # 2,3,4 in the XY plane between the #1 Rx antenna and the target tag, error along Z axis is significantly higher.

6.4 Localization with various scatters

To further show the robustness of the proposed method, 3D localization under various metal scatterers made of aluminum balls with diameter around 15 cm and soda cans of
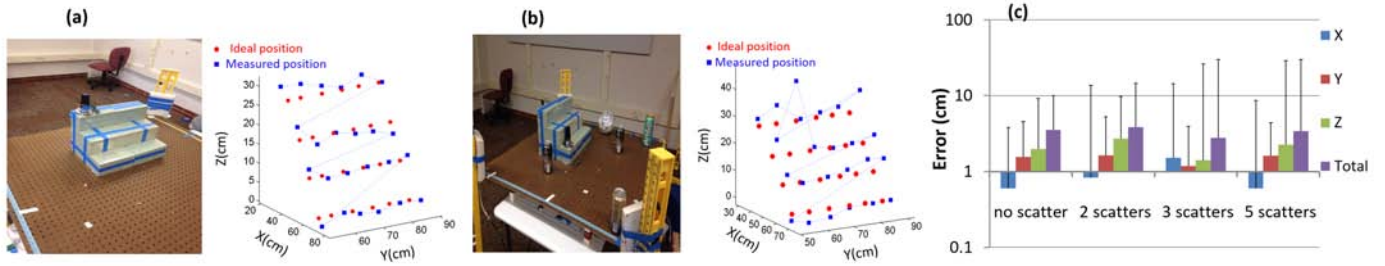
Figure 15: Testing samples of 3D localization in (a) scatterer-free and (b) 5 metal scatterers scenarios. (c) Median and maximum errors with different number of scatterers.
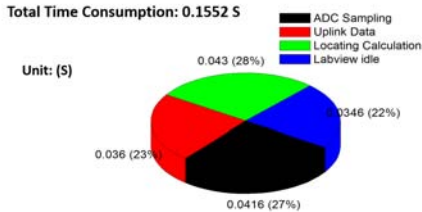

Figure 16: Pie chart of time latency for one 3D localization measurement

heights from 10 cm to 20 cm within the reading zone was performed. The metal scatterers were randomly distributed on the table among the TX and RX antennas. A sample measurement with 5 scatterers is shown in Fig. 15(b) in comparison with the scatterer-free case in Fig. 15(a). The measured median and maximum errors for scatterer-free, 2 scatterers, 3 scatterers and 5 scatterers are shown in Fig. 15(c). The outliers with above $10cm$ localization errors all have wrong cycle integer estimation when the multi-path phase errors are beyond our current system tolerance. The median errors all fell within centimeter range due to the accurate phase cycle integer solution. There was no obvious relationship between the median errors and number of scatterers among the measurements, as when the phase cycle integer calculation are correct, the major error source came from the antenna phase center uncertainties which could vary during each calibration. Further integration with more receiver antennas or with beamforming capabilities to solve such problems will be in the future work [29].

6.5 Real-time 3D tracking

In contrast to approaches which relied on relative motion and were thus not suitable for real-time application due to high latency [6, 10, 14], our approach can compute real-time 3D location accurately. Currently, the latency of our system to compute one 3D location is 0.155 seconds. The pie-chart of time consumption is shown in Fig. 16. The HM-FCW ranging algorithm and 3D localization computation consume 0.043 second (28%). The ADC consumes 0.042 second (27%) while the uplink data communication took 0.036 second (23%) To ensure Labview running smoothly, an idle time of 0.035 second (22%) was also inserted.

The location sampling frequency can be further increased by running ADC sampling, uplink data communication and localization calculation in parallel, thus achieving location sampling rate above 13Hz. Two experiments were performed, in the first experiment, we built an "3D-mouse" moving in

air. Fig. 17 shows real-time tracking of the "3D-mouse" moving left, up, inward and circularly, respectively. In the experiment, the nonlinear RFID tag was connected to a broadband whip antenna to reduce the total system weight. In the second experiment, the tag was mounted on the top of a toy train and tracking was shown in Fig. 18. The Z-direction information (trajectory height) was denoted by color. Fig. 19 shows the tracking trajectory standard deviation for 10 loops. The localization error in Figs. 14 and 15 is calculated as the difference between ruler measurements and our reader measurements, which may contain bias and distortion. The trajectory deviation in Fig. 19 is a relative measurement and can show the ability of our system to separate two adjacent locations. Because our localization approach was based on resolving the phase cycle integer, the measurements was highly sensitive to location. We achieved standard deviation of 0.138, 0.258 and $0.262cm$ along X, Y and Z directions, respectively.

7. FURTHER DISCUSSIONS

As nonlinear backscatter is fundamentally different from conventional linear backscatter, several concerns need to be addressed. In this section, we briefly discuss issues and outlooks along its development path.

7.1 Legitimate use of the spectrum

7.1.1 Legality on the harmonic re-radiation

The proposed RFID tags are passive devices with operating power $< 1mW$ (not actively radiating but only backscattering on the harmonics). For such passive tags, FCC regulation states that "a passive tag does not contain battery is not certified individually" and "only the reader needs to be tested" [35]. The interference from our harmonic backscattering to cellular bands is minimal and conforms to regulation. For the interference from the cellular bands to our receiver, more studies are needed, and we are currently investigating frequency hopping and orthogonal code injection.

7.1.2 Legality on the reader

The issue of sending multiple fundamental frequencies can be addressed by utilizing multi-band HMFCW ranging[20] to fit the present FCC regulation (e.g. by using two ISM bands). Recently, more opportunities arise from white space and other un-licensed uses which are opened up by FCC to provide more robust local access. For example, FCC now allows unlicensed use in the 5GHz band [36]. On November 4, 2008 FCC approved Report & Order 08-260, allowing unlicensed use of TV band spectrum [37]. When IoT and
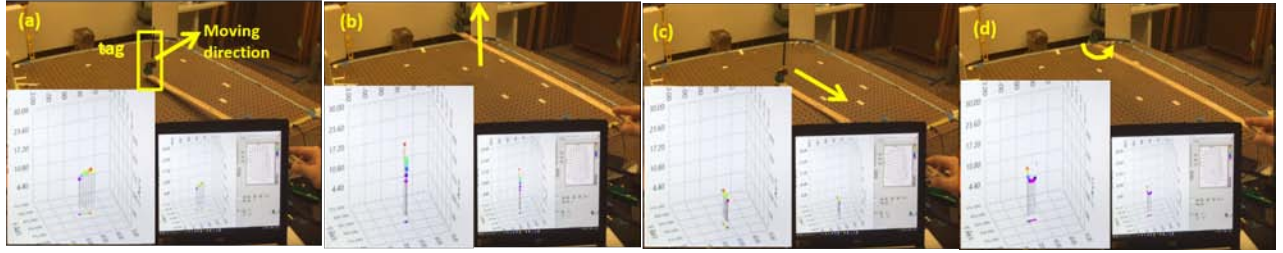
Figure 17: 3D-mouse tracking: (a) moving left; (b) moving up; (c) moving inward; (d) moving circularly.

Table 2: Optimal Tx frequency combination using multi-band HMFCW ranging

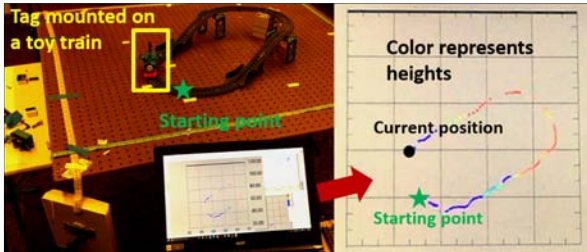| Bands	No. of freq.	Freq. (MHz)	Phase error threshold Φ	Reading range R
Dual ISM bands	5	910 928 2400 2461 2474	$21°$	4 m
TV white space & ISM bands	10	928 916 908 698 631 624 579 551 521 470	$56.5°$	4 m

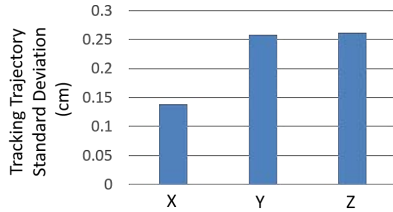Figure 18: Real-time 3D tracking of a passive tag attached to a toy train.

Figure 19: Tracking trajectory standard deviation.

proximity intelligence expand their applications in the future, further spectral choices can be possible. As the present demonstration is our experimental prototype, we selected the frequencies for proof of concepts, partially because the RF components in these bands are available commercially for board-level designs of our harmonic reader. For future development, we have more design freedom on the desirable bands in a custom IC solution. Multi-band HMFCW ranging operation [20] is similar to single-band HMFCW ranging. Given the frequency constraint, we can optimize the phase error threshold $\Phi(\mathbf{F}, K, R)$ defined in Eq. (17) by heuristic optimization. Using these white-space channels and ISM bands in Table. 2, we can achieve phase error threshold as large as $56.5°$.

7.2 Limitations on the reading range

For nonlinear backscatter with large separation of uplink and downlink frequencies, the received noise floor is fundamentally determined by the thermal noise instead of the phase noise skirt from the transmitter. The receiver noise floor is hence determined by the following equation [42]:

$$Noise\ Floor = -174dBm/Hz + NF + 10\log(B) \quad (23)$$

As data modulation is not required to separate the received signal from un-modulated reader inquiry signal, the bandwidth B could be designed to be small due to the low data rate a typical RFID requires. Consider a noise figure (NF) of $15dB$ for a common receiver and a $1KHz$ bandwidth, the noise floor of the receiver theoretically can be as low as $-129dBm$. In fact, today's GPS receiver generally has sensitivity about $-160dBm$ [38]. The reading range can be further increased with smaller B, better NF, and higher harmonic backscatter power, which could lead to a reading range much larger than $10m$. When data communication is required for tag ID information, similar to today's passive UHF RFID system, the reading range is most often limited by the downlink (reader-to-tag) due to the low efficiency for the RF-to-DC converter on the passive tag. However, recent progress in the IC research community reported a passive tag with RF-to-DC conversion sensitivity as low as $-34dBm$, which would drastically increase downlink reading range in the near future [39]. However, to meet the theoretical receiving noise floor, careful design in receiving architecture needs to be taken. Homodyne receivers, although simple, have several limitations as discussed in [43]. We expect significant improvement for the reading range when switching to a heterodyne receiver architecture [42]

7.3 Cost of nonlinear backscatter technology

For the nonlinear tags, if we consider the board-level implementation as in WISP, the additional discrete components will add about $1-2 for the additional BOM. In the future, when the nonlinear tag is implemented on CMOS IC, the cost is determined by the die area. Current RFID tag die has size typically about $0.5mm \times 0.5mm$ which corresponds to cost about $0.1 [40]. The NLTL is CMOS compatible and can be designed in an compact area of $0.35mm \times 0.6mm$ [41]. The additional area will add another $0.1 to $0.2 for each tag. It is possible that the entire NLTL can be on the top two metal layers and overlaid with the digital part, where the cost increment will then be minimal.

8. CONCLUSIONS

In this work, we show that real-time centimeter-accuracy 3D localization can be achieved for RFID with the nonlinear backscatter approach. Our present setup can achieve 3.5cm 3D localization accuracy and 0.155 seconds latency. Compared to previous work, the proposed approach does not need any relative motion or anchor nodes and therefore can be readily applied to a large variety of applications.

9. REFERENCES

[1] L. M. Ni, Y. Liu, Y. C. Lau and A. P. Patil. Landmarc: indoor location sensing using active RFID. In *IEEE Percom*, 2003.

[2] J. Zhou and J. Shi. RFID localization algorithm and applications, a review. *J. Intell. Manuf.*, 20(6):695–707, Dec. 2009.

[3] P. Nikitin, R. Martinez, S. Ramanurthy, H. Leland, G. Spiess and K. V. R. Rao. Phase based spatial identification of UHF RFID tags. In *IEEE RFID*, 2010.

[4] C. Xu, et al. Improving rf-based device-free passive localization in cluttered indoor environment through probabilistic classification methods. In *IPSN*, 2012.

[5] S. Radiom, et al. Far-field on-chip antennas monolithically integrated in a wireless-powered 5.8-ghz downlink/uwb uplink rfid tag in 0.18-um standard cmos. *IEEE Journal of Solid State Circuits*, 45(9):1746-1758, Sept. 2010.

[6] L. Yang, Y. Chen, X. Li, C. Xiao, M. Li and Y. Liu. Tagoram: Real-time tracking of mobile RFID tags to high precision using cots devices. In *ACM Mobicom*, 2014.

[7] J. Wang, D. Vasisht and D. Katabi. RF-IDraw: virtual touch screen in the air using RF signals. In *ACM Sigcomm*, 2014.

[8] C. H. Williams, B. Grant, X. Liu, Z. Zhang and P. Kumarl. Accurate localization of RFID tags using phase difference. In *IEEE RFID*, 2010.

[9] D. Arnitz, K. Witrisal and U. Muehlmann. Multi-frequency continuous-wave radar approach to ranging in passive UHF RFID. *IEEE Tran. Microw. Theory Tech.*, 57(5):1398–1405, May 2009.

[10] J. Wang, F. Alib, R. Knepper, D. Katabi and D. Rus. RF-compass: Robot object manipulation using RFIDs. In *ACM Mobicom*, 2013.

[11] T. Li, C. An, Z. Tian, A. T. Campbell and X. Zhou. Human sensing using visible light communication. In *ACM Mobicom*, 2014.

[12] L. Liu, et al. Anchor-free backscatter positioning for RFID tags with high accuracy. In *IEEE INFOCOM*, 2014.

[13] S. Lanzisera, D. Lin and K. S. J. Pister. RF time of flight ranging for wireless sensor networks localization. In *Workshop on Intelligent Solutions in Embedded Systems. Dig.*, 2006.

[14] R. Miesen, et al. Holographic localization of passive UHF RFID transponders. In *IEEE RFID*, 2011.

[15] J. Wang and D. Katabi. Dude, where is my card? RFID positioning that works with multipath and non-line of sight. In *ACM Sigcomm*, 2013.

[16] J. Fitch. Synthetic Aperture Radar. 1988.

[17] G. Durgin, et al. Modulation and sensitivity limits for backscatter receivers. In *IEEE RFID*, 2013.

[18] S. Lee, et al. A new TX leakage-suppression technique for an RFID receiver using a dead-zone amplifier. In *ISSCC Tech. Dig.*, 2013.

[19] D. M. Pozar. *Microwave Engineering*. 2011.

[20] Y. Ma and E. C. Kan. Accurate Indoor Ranging by Broadband Harmonic Generation in Passive NLTL Backscatter Tags. *IEEE Tran. Microw. Theory Tech.*, 2014.

[21] G. Li, D. Amitz, R. Ebelt, U. Muehlmann, K. Witrisal and M. Vossiek. Bandwidth dependence of CW radar ranging to UHF RFID tags in severe multipath environments. In *IEEE RFID*, 2011.

[22] T.H. Lee. *The Design of CMOS Radio-frequency Integrated Circuits*. 1998.

[23] http://www.impinj.com/products/readers. 2016.

[24] F. Yu, K. G. Lyon and E. C. Kan. A novel passive RFID transponder using harmonic generation of nonlinear transmission lines. *IEEE Tran. Microw. Theory Tech.*, 2010.

[25] W. Lee and E. Afshari. Low noise resonant parametric amplifier. *IEEE Tran. Circuits Syst.*, 2011.

[26] E. Afshari, H. S. Bhat, A. Hajimiri and J. E. Marsden. Extremely wideband signal shaping using one- and two-dimensional nonuniform nonlinear transmission lines. *Journal of Applied Physics*, 2006.

[27] Wisp 5 firmware repository. http://www.github.com/wisp/, 2016.

[28] X. Li, Y. Zhang and M. G. Amin. Multi-frequency-based range estimation of RFID tags. In *IEEE RFID*, 2009.

[29] J. Xiong and K. Jamieson. Arraytrack: A fine-grained indoor location system. In *NSDI*, 2013.

[30] S. Azzouzi et al. New measurement results for the localization of UHF RFID transponders using an angle of arrival (AoA) approach. In *RFID*, 2011.

[31] P.V. Nikitin and K.V.S Rao. Theory and measurement of backscattering from RFID tags. *IEEE Antennas and Propagation Magazine*, 2008.

[32] P.N. Betjes. An algorithm for automated phase center determination and its implementation. In *Proc. AMTA Conf.*, 2007.

[33] http://taoglas.com/images/product_images/original_images/TL.10.1HH11.pdf.

[34] http://taoglas.com/images/product_images/original_images/TG.22.0111.pdf

[35] New policies for part 15 devices. https://transition.fcc.gov/oet/ea/presentations/files/may05/New_Policies_Pt._15_SD.pdf, 2005.

[36] FCC increases availability of spectrum for high-speed, high-capacity wi-fi and other unlicensed uses in the 5GHz band. https://apps.fcc.gov/edocs_public/attachmatch/DOC-326341A1.pdf, 2014.

[37] FCC. https://apps.fcc.gov/edocs_public/attachmatch/FCC-08-260A1.pdf, 2008.

[38] http://www.canadagps.com/KB_04.html, 2016.

[39] J. Kang, P. Y. Chiang and A. Natarajan. A 1.2cm2 2.4GHz self-oscillating rectifier antenna achieving -34.5dBm sensitivity for wirelessly powered sensors. In *Digest of ISSCC*, 2016.

[40] NXP SL3S1204. http://www.nxp.com/documents/data_sheet/SL3S1204.pdf, 2016.

[41] F. Yu, Y. Ma and E. C. Kan. Reflective nonlinear transmission lines for single-antenna non-self-jamming RFID. In *IEEE International Microwave Symposium*, 2011.

[42] B. Razavi. *RF Microelectronics*. Prentice Hall, 1998.

[43] B. Razavi. Design considerations for direct-conversion receivers. *IEEE Transactions on Circuits and Systems II*, 1997.

[44] J. R. Shewchuk An introduction to conjugate gradient method without the agonizing pain. 1994.

[45] D. Bharadia, Emily. McMilin and S. Katti Full duplex radios. In *ACM Sigcomm*, 2013.